Optics Letters

3D laser-written silica glass step-index high-contrast waveguides for the 3.5 μm mid-infrared range

Javier Martínez,[1] Airán Ródenas,[1,*] Toney Fernandez,[2,5] Javier R. Vázquez de Aldana,[3] Robert R. Thomson,[4] Magdalena Aguiló,[1] Ajoy K. Kar,[4] Javier Solis,[2] and Francesc Díaz[1]

[1]Física i Cristal•lografia de Materials (FiCMA), Departament de Química Física i Inorgànica, Universitat Rovira i Virgili, 43007 Tarragona, Spain
[2]Laser Processing Group, Instituto de Óptica-CSIC, Madrid 28006, Spain
[3]Laser Microprocessing Group, Facultad de Ciencias, Universidad de Salamanca, 37008 Salamanca, Spain
[4]Institute of Photonics and Quantum Sciences, Heriot-Watt University, Edinburgh EH14 4AS, UK
[5]Currently at Dipartimento di Fisica, Politecnico di Milano, Milano, Italy
*Corresponding author: arodenas@gmail.com

Received 21 September 2015; revised 17 November 2015; accepted 17 November 2015; posted 19 November 2015 (Doc. ID 250479); published 11 December 2015

We report on the direct laser fabrication of step-index waveguides in fused silica substrates for operation in the 3.5 μm mid-infrared wavelength range. We demonstrate core-cladding index contrasts of 0.7% at 3.39 μm and propagation losses of 1.3 (6.5) dB/cm at 3.39 (3.68) μm, close to the intrinsic losses of the glass. We also report on the existence of three different laser modified SiO_2 glass volumes, their different micro-Raman spectra, and their different temperature-dependent populations of color centers, tentatively clarifying the SiO_2 lattice changes that are related to the large index changes. © 2015 Optical Society of America

OCIS codes: (130.2755) Glass waveguides; (140.3390) Laser materials processing; (220.4000) Microstructure fabrication.

http://dx.doi.org/10.1364/OL.40.005818

The advent of intersubband cascade lasers in the mid-90s [1–3] and of interband cascade lasers (ICL) more recently [4] played a crucial role in the development of mid-infrared (IR) optical instruments (from around 2.5 to 20 μm) [5]. Likewise, due to the high interest in deploying remote mid-IR sensors, huge work has also been done in the field of fiber growth, with fluoride and chalcogenide glasses as the most widespread solid-fiber materials [6–8]. Yet these glasses have mechanical and corrosion limitations that make them unsuitable for long exposure to the environment. Chalcogenide glasses have a much lower fracture stress limit than fused silica glass, are susceptible to water corrosion, have low optical-damage thresholds, and typically have toxic arsenic as a primary component. Fluoride glasses also share similar mechanical, water-corrosion, and optical-damage limitations [9]. Fused silica glass on the other hand is well known to be mechanically and thermally resilient; chemically resistant to nonfluorinated acids, solvents, or plasmas; and is currently ubiquitous in many industries, from optical fibers to microfluidic systems, microelectromechanical systems (MEMS), high temperature glassware, microscope slides, or in thermonuclear reactors as long-lifetime vacuum windows capable of withstanding high neutron and gamma irradiation levels [10–12]. Fused silica glass is, however, also frequently thought to be "opaque" for wavelengths above around 2.5 μm, though this is not the case for high-purity fused silica glass, which maintains its high transparency to around 3.5 μm wavelength. Since novel surface-sensing schemes based on dielectric loaded plasmonics [13] allow for short optical path lengths, the benefits of having a robust fused-silica-glass chip as a light loading interface for point sensing could outweigh the limitations of intrinsic absorption losses of the material. In this Letter, we explore the fabrication of 3D waveguides (WGs) inside silica for single-mode operation around 3.5 μm wavelength, with capability for bends with radii below 15 mm, and low numerical aperture so as to provide low-loss fiber interconnects.

To have embedded WGs with 3D architectures capable of interconnecting fibers as well as having on-chip functional WG circuits, the 3D direct laser writing technique (DLW) has become the standard technique after almost 20 years of research, with fused silica being the most frequently studied material [14–20]. Our DLW setup consisted of an fs-fiber-laser amplifier (Tangerine, Amplitude Systemes) delivering ~450 fs pulses at 1047 nm and at a rate of 500 KHz. The laser power was kept at 400 mW by means of neutral density filters, and the beam was circularly polarized. The laser beam was focused inside Suprasil 300 (S300, Heraeus) high-purity silica using an aspheric lens with 0.4 NA. The sample was translated at a speed of 1.5 mm/s, and the multiscan approach was used [16], with a scan separation of 0.4 μm. For this work, we performed a study of WG depth fabrications down to 1480 μm so as to evaluate the potential for inscribing "on the fly" 3D circuits. After WG fabrication, the sample facets were polished to optical quality, characterized under bright-field microscopy, and characterized in a mid-IR guiding setup. Our guiding setup consisted of a 1.5 mW HeNe laser (3.39 μm) and a 3 mW ICL tunable laser (from 3.57 to 3.68 μm). Both lasers provided vertically polarized beams. A pair of lenses with NA = 0.18 (Thorlabs

C021TME-E) were used for in- and out-coupling laser light from the WGs. A Thorlabs (PDA20H-EC) PbSe amplified detector was used in combination with a FLIR SC700 camera for imaging the output WG modes. COMSOL software was used to simulate the WGs modes assuming step-index profiles and the measured core sizes from bright-field microscopy: by changing the core refractive index, the simulated mode field diameters (MFDs) could be made to match the experimentally found values, therefore obtaining approximate inferred values for the core index changes $\Delta n = n_{\text{core}} - n_{\text{cladding}}$ for all WGs, where the n_{cladding} value is assumed to be the index of unmodified glass. Figure 1 shows a summary of the characterization results performed at 3.39 μm. Figure 1(a) shows the measured MFDs for horizontal (x) and vertical (y) directions and for 5 different WG depths. As can be seen, the MFDs only changed within ±1 μm for all depths. Figure 1(b) shows the near-field images of the 5 WGs and the MFDs vertical to horizontal ratios (R). The mode ratios are measured to be almost constant at $R = 1 \pm 5\%$, which is fundamental for ensuring low-loss coupling to optical fibers. Figure 1(c) shows the bright-field images of the WGs at different depths. Three different zones observed in the WGs are labeled II, I, and I*. The first two zones (II and I) are believed to correspond to Type II and Type I index modifications, respectively [21,22]. Type I modifications consist of index increased volumes, and Type II regions are typically depressed index zones with nanoscale features. The core waveguiding region is therefore assumed to be only zone I and I*. Finally, Fig. 1(d) shows the corresponding estimated mid-infrared Δn values for different fabrication depths, which on average is of 0.01 ± 0.0015.

The estimated NA of these WGs, $\text{NA} = (n_{\text{core}}^2 - n_{\text{clad}}^2)^{1/2}$, is NA ~ 0.17, therefore allowing for low-loss coupling to commercial fluoride optical fibers, which adds to the advantage of reduced Fresnel losses between fused silica and fluoride glasses. Importantly, an index change of $\Delta n = 0.01$ with the low cladding index of 1.4095 of silica at 3.39 μm indicates that these WGs have a high index contrast $C\% = \Delta n / n_{\text{core}}$ of ~0.7%, a value significantly high for a DLW WG. This contrast value at 3.39 μm is higher than other previously reported values for mid-infrared DLW WGs in chalcogenide glass (~0.55%) [23] and borate crystals (~0.29%) [24], allowing for tighter bend radii without significant losses. It is also appropriate to indicate here that although the typical values found in the literature for the Δn of multiscan DLW WGs in silica are lower at around ~2E − 3 [25], these values are typically measured at visible or near-infrared wavelengths, far from the long-wavelength transmission edge of silica, which is associated to multiphonon excitations. In this sense, a straight comparison with previously reported Δn values can therefore be misleading [26]. The significance of this high index contrast of ~0.7% with step-index WGs was estimated by performing a comparison of two equivalent s-bent WGs using the beam propagation method (BPM). The simulation of a WG with core size of 13 μm, $\Delta n = 0.01$ and a normalized frequency parameter $V = 2.026$, which for two s-bends with radii of 15 mm yielded a total radiation loss of only 0.5 dB, whereas a step-index WG with the same V parameter but a standard index of $\Delta n = 2\text{E} - 3$ would lose all the light at the start of the first bend. The reported WGs therefore allow for smaller DLW footprint circuits than previously envisaged, thus allowing for shorter optical paths and therefore significantly reduced propagation losses at mid-IR wavelengths than previously thought for silica WGs.

The insertion losses (IL) were measured for all the WGs. The coupling losses (CL) were estimated using the overlap integral between the measured WG mode and the measured focal spot of the input/output lenses. The propagation losses (PL) were then obtained from $\text{PL} = (\text{IL} - 2\text{CL})/L$, where L is the WG length. Figure 2 shows the measured transmission spectrum of the S300 sample and the WG PLs of WGs fabricated at 550 μm depth. The PLs follow closely the transmission of S300, being of 1.3 (6.5) dB/cm at 3.39 (3.68) μm wavelength. To evaluate the thermal resistance of the WGs, the sample was submitted to a two-step annealing process: a first annealing step for 2 h at 200°C and a second one at 400°C were performed. After the annealing, the WGs were found to be almost unchanged, the index change was found to be maintained within the ±1E − 3 error, and only the PL at 3.68 μm was observed to slightly deteriorate by +0.55 dB/cm. The fact the WG PLs are 0.5 dB larger than the glass intrinsic absorption at 3.39 μm, and even 1.0 dB larger at the longer wavelength of 3.68 μm, suggests that a larger mode would have a further extension in the defect zone I, where light scattering and absorption is likely to occur. To better understand the morphology of the multiscan WGs, a detailed analysis of the WGs was performed. Figure 3 shows optical bright-field, back-scattered electrons (BSE), and secondary electrons (SE) micrographs of the WG output facet. These images allow to better differentiate volume II (nanostructured defects region), I (index increased core), and I*. The BSE

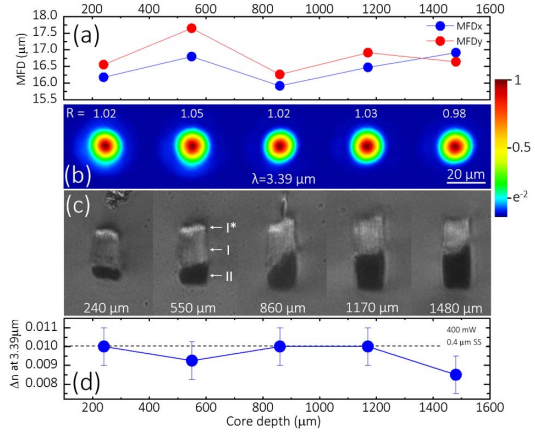

Fig. 1. (a) Horizontal (x) and vertical (y) mode field diameters, (b) output near-field images, (c) bright-field transmission images of WGs, (d) inferred approximate core index changes.

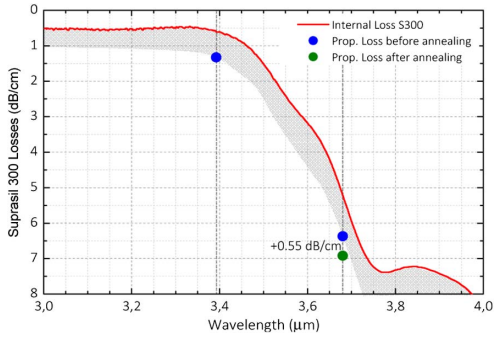

Fig. 2. Measured transmission spectrum of S300 sample together with the WG propagation loss values at different wavelengths.

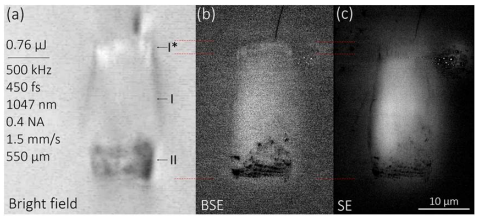

Fig. 3. (a) Optical bright-field, (b) back-scattered electrons, and (c) secondary electrons images of a WG. Volumes II, I, and I* indicated.

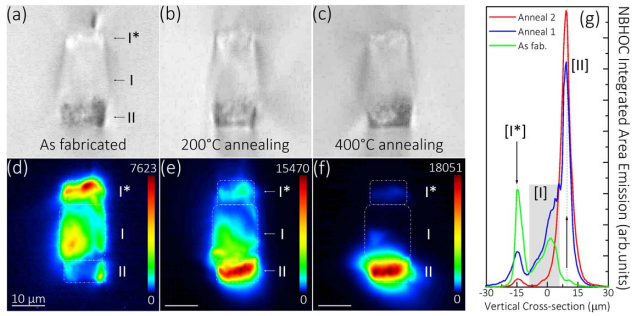

Fig. 5. (a, d) As fabricated WG, (b, e) after 200°C first annealing, (c, f) 400°C second annealing, (g) vertical cross-sections of the three maps.

image shows that the core region I + I* corresponds to densified SiO_2 glass due to the increased brightness. Densification is therefore a main contribution to the large observed mid-infrared index increase.

Further information on the performed laser micromodifications can be obtained from microspectroscopy mapping of the WG facet. With this aim, we first performed micro-Raman confocal measurements at the center of the WG core (zone I) and in unmodified glass volume (see Ref. [23] for further experimental setup details). Figure 4 shows the Raman and luminescence spectra obtained at three different excitation wavelengths. Gaussian fits were used to deconvolute the different broad emission bands of luminescent centers. Excitation at 514 nm [Fig. 4(e)] in unmodified S300 produces broad emission of oxygen deficiency centers (ODCs) with peak intensity at 546 nm (2.27 eV), as well as of an unidentified laser-induced defect (LID) at 576 nm (2.15 eV) [22]. At the WG core, however, strong emission from nonbridging oxygen-hole centers (NBOHCs) is also observed. When exciting at 532 nm [Fig. 4(b)], only NBOHC defects are observed to emit both from unmodified glass and from the WG core, although the peak intensity coming from the core is almost 20-fold more intense than from unmodified glass. Lastly, when exciting at 785 nm [Fig. 4(c)], no luminescence is observed, and the Raman spectrum can be accurately measured.

To obtain a better image of the presence and distribution of NBOHC defects, Fig. 5 presents luminescence 2D micromapping of the WG cross section performed before and after the annealing process, revealing that, in the as-fabricated WG NBOHC, defects are mostly present in the WG core with the highest concentration located at region I*, but after the two-step 400°C thermal annealing, NBOHCs are remarkably activated at region II (defect nanofeatures) and almost completely erased from other volumes, this being in line with previous observations by Mishchik *et al.*, even if they were performed at the low repetition rate regime and without multiscan overwriting [27]. Since the index change at the WGs was not observed to change significantly as a result of the annealing process, these experiments confirm that the mid-infrared Δn at the WG core (zone I) is not driven by the presence of NBOHCs, this observation being also in line with previous findings by Reichman *et al.* for the visible range [28]. The obtained mid-IR high index change would then be due at least to the higher glass density observed in the brighter BSE images [see Fig. 3(b)], while other lattice changes such as an increased polarizability could also contribute to the effect.

A micro-Raman mapping (see Fig. 6) was also performed in the WG, before and after annealings, to evaluate the phonon lattice changes produced at each modified volume. Results were very similar in both cases, so after-annealing results are not shown for the sake of brevity. Figure 6(k) shows representative spectra at unmodified S300 glass, top of the core (region I*), core (region I), and at the bottom (nanogratings) region II. The integrated area map of the broad R phonon band [Fig. 6(b)] shows a decrease of 26% from normal glass to zone II, but not at the positive index volumes, thus indicating that, at zone II (nanofeatures defects), indeed strong lattice defect creation

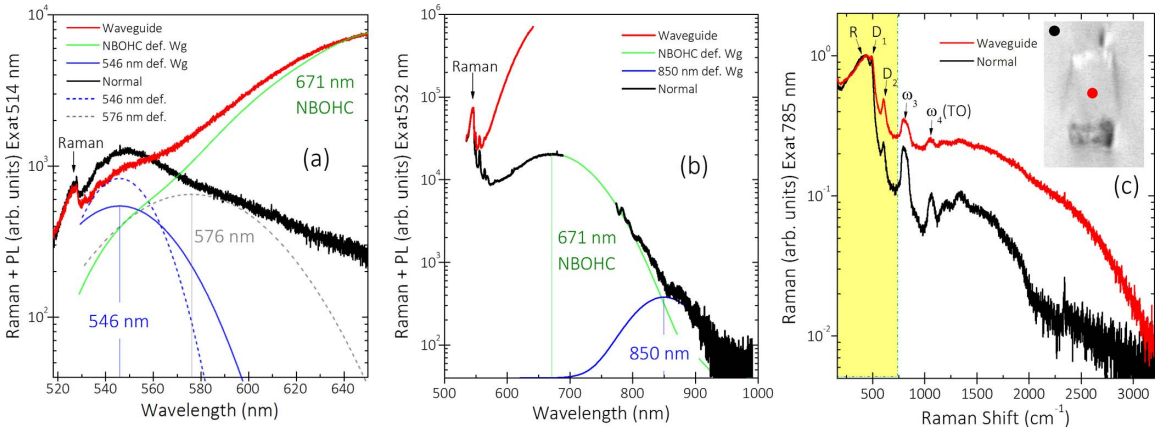

Fig. 4. Micro-Raman spectra inside and outside of the WG: (a) excitation at 514 nm yields a dominant emission of three color centers, (b) excitation at 532 nm yields Raman and emission from NBOHCs, (c) excitation at 785 nm yields clear Raman with no luminescence background. All graphs are in logarithmic scale for clarity of all spectral features.

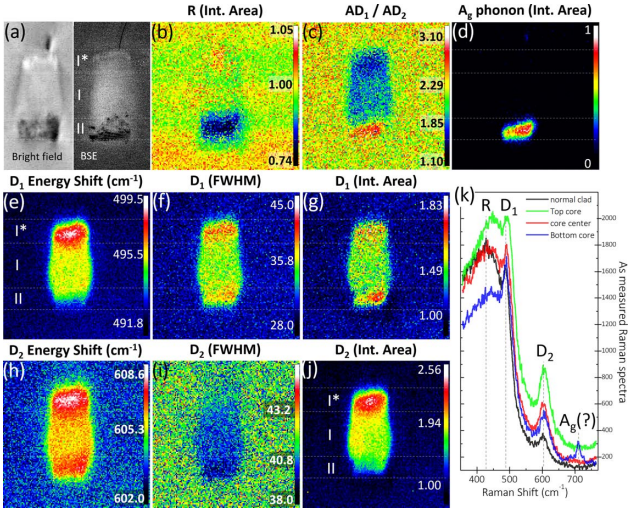

Fig. 6. (a) Bright-field and BSE images; (b) integrated area of R mode; (c) ratio of D_1 and D_2 modes areas; (d) area of the 707 cm^{-1} (A_g) mode; (e) and (h) energy shifts of D_1 and D_2, respectively; (f) and (i) FWHM of D_1 and D_2, resepectively; (g) and (j) areas of the D_1 and D_2, respectively; and (k) representative Raman spectra at nonmodified normal point and at each of the three modified zones.

occurs. This behavior is, however, not observed for the rest of phonon modes. A phonon at 707 cm^{-1} with narrow crystal-like full width at half-maximum (FWHM) of only 13.5 cm^{-1} is also detected at zone II only [Fig. 6(d)] (and which disappeared after 400°C annealing), indicating that indeed fundamental structural transformations of the SiO_2 glass structure occur at this nanostructured volume. This phonon has never been reported in SiO_2 glass to our knowledge, and we tentatively assign it to the identified A_g mode at 705 cm^{-1} from Si-O-Si characteristic bending vibrations of ordered SiO_2 polyhedra in Jadeite [29]. Figures 6(e)–6(j) show maps of phonon energy, FWHM, and integrated area of D_1 and D_2 ring modes. At regions I and I*, a blueshift of both D_1 and D_2 modes is observed, indicating a probable higher compaction level of these ring defects as compared to the surrounding glass and which could be also related to the observed index changes at the long wavelength limit of transparency of the glass, related to multiphonon absorptions. Finally, we also analyzed the ratio of integrated areas of D_1 and D_2 rings, finding a clear trend in which the depressed index zone II has a high ratio value of ∼3, while positive Δn zones I and I* show a lower value of ∼1.85 down to ∼1.1. The use of this ratio coefficient could prove useful as an indicator of refractive index increased areas in DLW fused silica glass. Further in depth analysis of these observations is being prepared and will be published elsewhere.

In conclusion, we have demonstrated the DLW of step-index WGs in SiO_2 glass capable of guiding at around the 3.5 μm range. We have proved these WGs can sustain temperatures of up to 400°C and can provide low-loss coupling to mid-IR fluoride fibers. We have also studied the microstructural changes associated with the femtosecond pulse laser modified glass, identifying three different states of SiO_2 glass state.

Funding. Spanish Government (MAT2013-47395-C4-4-R, TEC2014-55948-R, TEC2014-52642-C2-1-R, FIS2013-44174-P); Catalan Government (2009SGR235, 2014FI_B 00274); European Commission (EC) (ACP2-GA-2013-314335-JEDI ACE).

Acknowledgment. F. D. acknowledges additional support 2010ICREA-02 for excellence in research.

REFERENCES

1. J. Faist, F. Capasso, D. L. Sivco, C. Sirtori, A. L. Hutchinson, and A. Y. Cho, Science **264**, 5158 (1994).
2. Y. Yao, A. J. Hoffman, and C. F. Gmachl, Nat. Photonics **6**, 432 (2012).
3. M. S. Vitiello, G. Scalari, B. Williams, and P. De Natale, Opt. Express **23**, 5167 (2015).
4. W. Zeller, L. Naehle, P. Fuchs, F. Gerschuetz, L. Hildebrandt, and J. Koeth, Sensors **10**, 2492 (2010).
5. C. R. Webster, P. R. Mahaffy, S. K. Atreya, G. J. Flesch, and K. A. Farley, and the MSL Science Team, Science **342**, 355 (2013).
6. M. Saad, Proc. SPIE **7316**, 73160N (2009).
7. V. Fortin, M. Bernier, S. T. Bah, and R. Vallée, Opt. Lett. **40**, 2882 (2015).
8. B. Bureau, C. Boussard-Plédel, V. Nazabal, J. Adam, and J. Lucas, "Chalcogenide optical fibers for mid-infrared sensing: state of the art and future strategies," in *Advanced Photonics*, OSA Technical Digest (online) (Optical Society of America, 2014), paper SeTh1C.1.
9. N. Caron, M. Bernier, D. Faucher, and R. Vallée, Opt. Express **20**, 22188 (2012).
10. Y. Bellouard, A. Said, and P. Bado, Opt. Express **13**, 6635 (2005).
11. Y. Bellouard, Opt. Mater. Express **1**, 816 (2011).
12. I. I. Orlovskiy, K. Y. Vukolov, E. N. Andreenko, and T. R. Mukhammedzyanov, J. Nucl. Mater. **442**, S508, Supplement 1, 508 (2013).
13. B. Schwarz, P. Reiniger, D. Ristanic, H. Detz, A. M. Andrews, W. Schrenk, and G. Strasser, Nat. Commun. **5**, 4085 (2014).
14. K. M. Davis, K. Miura, N. Sugimoto, and K. Hirao, Opt. Lett. **21**, 1729 (1996).
15. A. Marcinkevičius, S. Juodkazis, M. Watanabe, M. Miwa, S. Matsuo, H. Misawa, and J. Nishii, Opt. Lett. **26**, 277 (2001).
16. Y. Nasu, M. Kohtoku, and Y. Hibino, Opt. Lett. **30**, 723 (2005).
17. G. D. Marshall, M. Ams, and M. J. Withford, Opt. Lett. **31**, 2690 (2006).
18. R. R. Thomson, H. T. Bookey, N. D. Psaila, A. Fender, S. Campbell, W. N. MacPherson, J. S. Barton, D. T. Reid, and A. K. Kar, Opt. Express **15**, 11691 (2007).
19. S. J. Beecher, R. R. Thomson, B. P. Pal, and A. K. Kar, IEEE Sens. J. **12**, 1263 (2012).
20. G. Cheng, C. D'Amico, X. Liu, and R. Stoian, Opt. Lett. **38**, 1924 (2013).
21. Y. Shimotsuma, P. G. Kazansky, J. Qiu, and K. Hirao, Phys. Rev. Lett. **91**, 247405 (2003).
22. R. Stoian, K. Mishchik, G. Cheng, C. Mauclair, C. D'Amico, J. P. Colombier, and M. Zamfirescu, Opt. Mater. Express **3**, 1755 (2013).
23. A. Ródenas, G. Martin, B. Arezki, N. Psaila, G. Jose, A. Jha, L. Labadie, P. Kern, A. Kar, and R. Thomson, Opt. Lett. **37**, 392 (2012).
24. A. Rodenas and A. K. Kar, Opt. Express **19**, 17820 (2011).
25. W. Watanabe, Y. Note, and K. Itoh, Opt. Lett. **30**, 2888 (2005).
26. S. M. Eaton, M. L. Ng, R. Osellame, and P. R. Herman, J. Non-Cryst. Solids **357**, 2387 (2011).
27. K. Mishchik, C. D'Amico, P. K. Velpula, C. Mauclair, A. Boukenter, Y. Ouerdane, and R. Stoian, J. Appl. Phys. **114**, 133502 (2013).
28. W. J. Reichman, D. M. Krol, L. Shah, F. Yoshino, A. Arai, S. M. Eaton, and P. R. Herman, J. Appl. Phys. **99**, 123112 (2006).
29. M. Prencipe, J. Raman Spectrosc. **43**, 1567 (2012).